Eur. Phys. J. Plus (2016) **131**: 109
DOI 10.1140/epjp/i2016-16109-4

THE EUROPEAN PHYSICAL JOURNAL PLUS

Regular Article

Dynamics of a vibrational energy harvester with a bistable beam: voltage response identification by multiscale entropy and "0-1" test

P. Harris[1], C.R. Bowen[1], H.A. Kim[2], and G. Litak[3,4,a]

[1] Department of Mechanical Engineering, University of Bath, Bath, BA2 7AY, UK
[2] Structural Engineering, Jacobs School of Engineering, University of California, San Diego, 9500 Gilman Drive, La Jolla, CA 92093, USA
[3] Faculty of Mechanical Engineering, Lublin University of Technology, Nadbystrzycka 36, 20-807 Lublin, Poland
[4] Laboratoire de Génie Electrique et Ferroélectricité, Institut National des Sciences Appliquées de Lyon, 8 rue de la Physique, 69621 Villeurbanne Cedex, France

Received: 28 August 2015 / Revised: 22 February 2016
Published online: 21 April 2016

Abstract. The use of bistable laminates is a potential approach to realize broadband piezoelectric-based energy harvesting by introducing elastic non-linearities to the system. In this paper the dynamic response of a piezoelectric material attached to a bistable laminate beam is examined based on the experimental measurement of the generated voltage-time series. The system was subjected to harmonic excitations and exhibited single-well and snap-through vibrations of both periodic and chaotic character. The ability to identify the vibration modes of the energy harvester is important since different levels of power are expected in each dynamic mode. We identify the dynamics of the selected system response using return maps, multiscale entropy, and "0-1" test. The potential of the approaches to identify periodic and chaotic modes and snap-through events in the non-linear bistable harvester is described.

1 Introduction

The use of energy harvesting to convert mechanical vibration into electrical energy is of interest for a variety of applications such as battery-free wireless sensor networks, safety monitoring devices, self-powered low-power electronics or simply to recharge storage devices such as batteries and capacitors [1]. Vibration energy harvesting can allow autonomous operation, provide environmental benefits due to reduced battery usage, battery disposal and alleviate maintenance costs, especially for sensors operating in harsh environments or those placed in inaccessible locations.

In a number of cases the source of the ambient vibrations being harvested can exhibit multiple and time-dependent frequencies. The nature of the vibration can also change with time and can include components at low frequencies [2]. Since the vibrations being harvested are rarely of fixed frequency it is therefore inefficient to employ devices with a high quality factor (Q) that operate at a resonant frequency; for example, simple linear cantilever configurations coupled to piezoelectric transducers.

There have been a number of attempts to broaden the frequency response of vibration energy harvesters by introducing elastic non-linearities into the harvesting system [2–5]. This includes the design of bistable structures which exhibit two specific energy wells and can oscillate between two stable states. Methods to generate bistability include the use of repulsive or attractive magnetic interactions between a cantilever and an external magnet, axial loading and the use of post-buckled beams [4].

An alternative method of achieving bistability in an energy harvester was initially reported by Arrieta *et al.* [6] where a piezoelectric element was attached to an asymmetric bistable laminate plate made from a carbon fibre reinforced polymer (CFRP) with a $[0/90]_T$ layup. The bistability in such a material originates from the asymmetric laminate

[a] e-mail: g.litak@pollub.pl (corresponding author)

layup and differences in the thermal expansion coefficient between the carbon fibre and epoxy matrix that generate thermal residual stresses on cooling the laminate from an elevated cure temperature.

When subjected to large-amplitude oscillations the bistable laminate can undergo snap-through between the two stable states [7,8] leading to a large deformation of any piezoelectric material attached to the laminate. Such harvesting structures have been shown to exhibit high levels of power extraction over a wide range of frequencies [6, 7]. The advantages of using the intrinsic thermal stress in the laminate to induce bistability, compared to using magnetic configurations [6–8], is that i) the arrangement can be designed to occupy a smaller space, ii) there are no stray magnetic fields, iii) the laminate can be readily combined with piezoelectric materials and iv) there is potential to tailor the laminate lay-up, laminate elastic properties by choice of the pre-preg material and geometry to provide additional control over the harvester response to the vibrations that are being harvested.

Initial research of bistable laminates for vibration harvesting examined centrally mounted laminate plates as the geometry for harvesting [6, 9–20]. Recently, interest has focused on cantilever configurations [7, 8, 21, 22] and even arbitrary shapes [23]. The cantilever configuration is of interest for broadband energy harvesting since large strains are developed near the clamped end of the structure and snap-through events can be achieved at relatively low vibration levels compared to unconstrained laminate plates [8].

In this paper a bistable asymmetric laminate in a cantilever configuration is manufactured and coupled to a ferroelectric material for energy harvesting applications. The cantilever configuration will be explored for energy harvesting and the time histories of velocity and voltage output as a function of vibration frequency at low and high vibration levels where the device exhibits either single well oscillations or snap-through events. To improve our understanding of the dynamic behaviour of the system, methods such as multiscale entropy analysis and "0-1" test are used with an aim to identify the system response. Understanding and identifying the vibration modes of the harvester is of importance since each mode can provide different power outputs [7]. For example, snap-through from one state to another is used to generate the highest power due to the largest deflection [7].

2 Experimental

In order to convert mechanical vibrations of the bistable laminate beams into electrical energy a Micro Fibre Composite (MFC) piezoelectric element (M8528-P2, Smart Materials) of dimensions 105 mm × 34 mm was bonded to the surface of the laminate at 35 mm from the root. The MFC is based on a lead zirconium titanate (PZT) ferroelectric ceramic which is polarised through its thickness with a manufacturer's specified capacitance C_p of 172 nF [22]. This is in contrast to most MFC configurations with an interdigital electrode (IDE) where the polarization direction is along the fibre length and is characterized by a low efficiency [24–26]. In this case the M8585-P2 device is polarised through thickness by continuous upper and lower electrodes. Compared to an IDE based device such a configuration has i) a more uniform electric field distribution ii) a high device capacitance, leading to low peak voltages as a result of the piezoelectric charge and iii) a low electrical impedance due to the high device capacitance.

The experimental setup together with beam clamping and location of the piezoceramic patch and laser scan point are presented in fig. 1. The bistable beam equilibria (state I and state II) are shown in fig. 2. The bistable property of the laminated beam is reflected in the softening system response in the area of resonance. In fig. 3 we show the sweep up (increasing frequency) and down (decreasing frequency) for the forcing acceleration amplitude of $a = 4g$ and $6g$. The resonance curve, for power output P_{out} is determined from

$$P_{\text{out}} = U_{\text{rms}}^2/R, \tag{1}$$

where U_{rms} denotes the root mean square of voltage and R is electrical resistance of the load resistor (36 kΩ). The resistor was chosen on the basis that the optimum load resistance fulfills at the condition $\omega RC_p = 1$ where $\omega = 2\pi f$ is angular frequency while the resonant frequency f is approximately 25 Hz.

The effects of the asymmetry of the double potential well of the elastic response of the cantilever on the power output is reflected in the bifurcations in the low frequency limit. Namely, on the left hand side of the resonance one can see the coexistence of two solutions —non-resonant and resonant ones— depending on the direction of the frequency sweep. Furthermore in case of $a = 6g$, just before the resonance frequency, one can clearly see the splitting of one solution into two of different power output (fig. 3), which corresponds to the appearance of resonant and non-resonant solutions. Around the resonance the single-well solutions, which are well defined in the low and high frequencies, bifurcate to periodic and non-periodic cross-well (snap-through) solutions.

In fig. 4 we show the time histories of velocity and voltage output concentrating on the typical solutions in the region of resonance. In fig. 4(a) we present the single well and periodic solution for a small amplitude of acceleration ($a = 4g$) and frequency of 16 Hz. Figures 4(b)–(d) correspond to the intermediate case with the forcing amplitude of $a = 5g$ and the frequencies $f = 16$, 17, and 25 Hz. The response at these conditions can be described as "snap-through" when the cantilever is undergoing transitions from state I to state II.

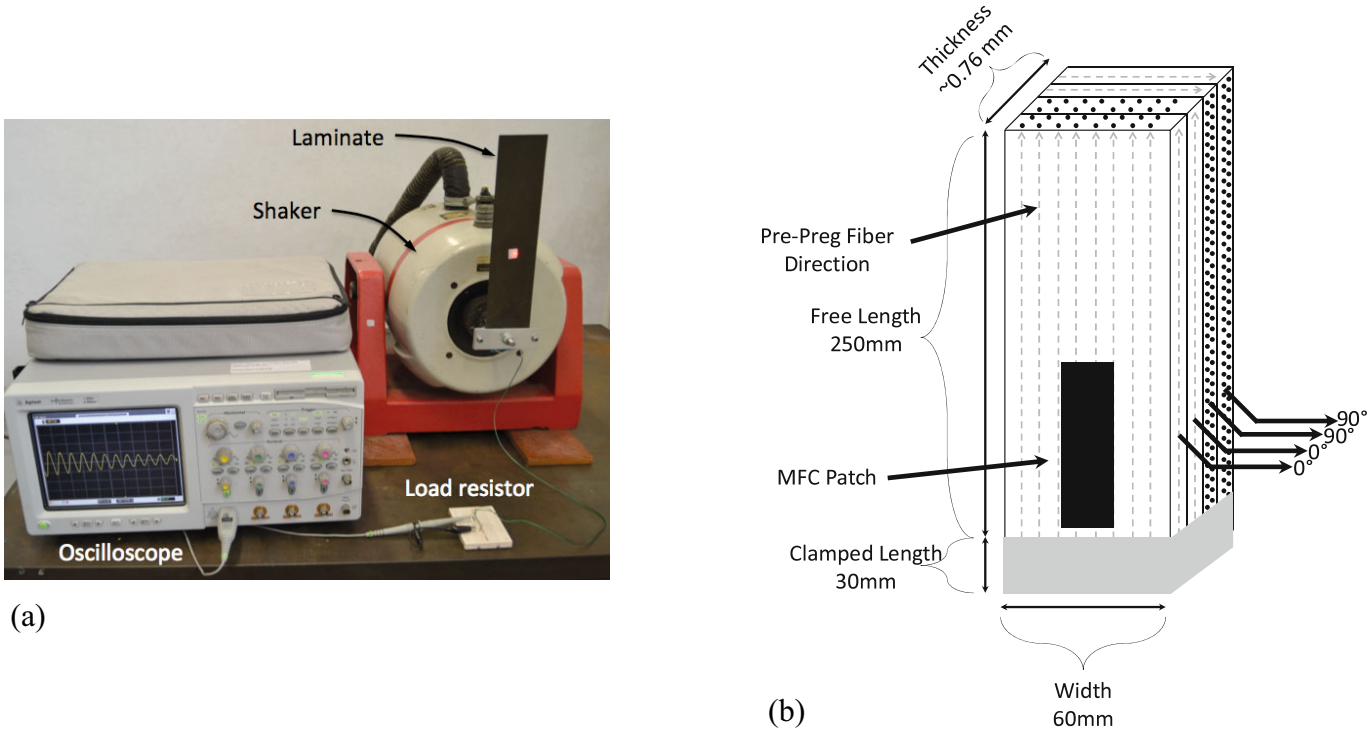

Fig. 1. (a) Experimental setup showing mechanical shaker attachment, the beam clamping and location of the piezoceramic patch and laser scan point. (b) Geometry of the bistable harvester.

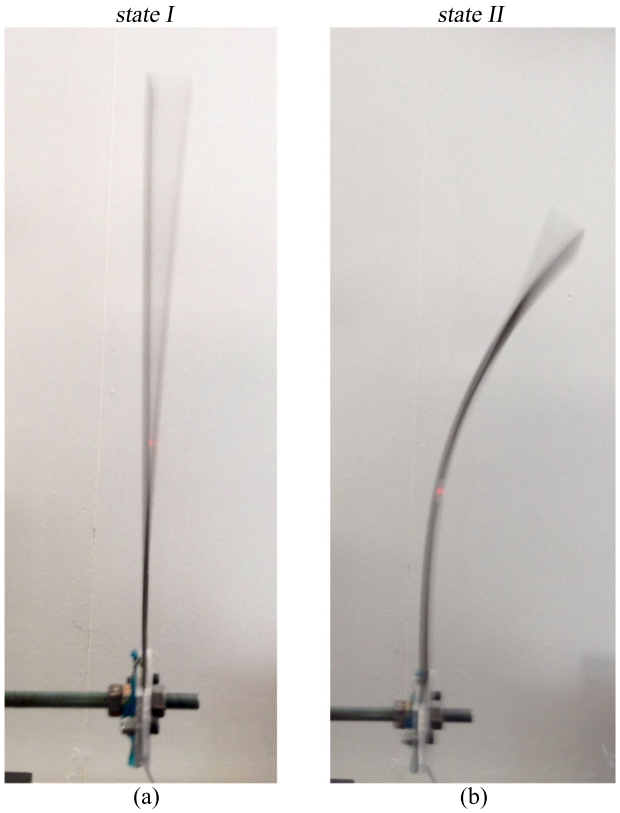

Fig. 2. Photo of the bistable laminate beam in small vibrations around the two equilibrium states. Cantilever length is 250 mm for scale.

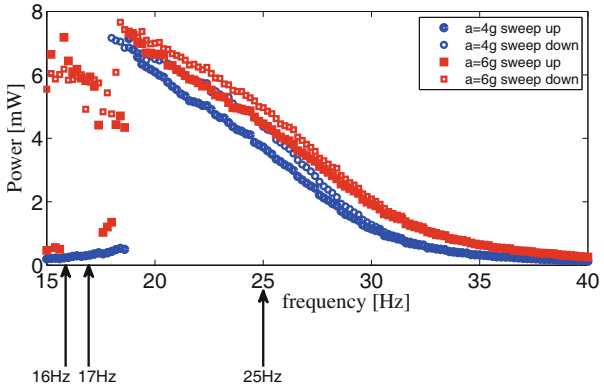

Fig. 3. Frequency sweeps up and down for the harmonic forcing acceleration amplitude $a = 4$ and $6g$ (with sweep up and sweep down, respectively). The power output was measured on a resistor $R = 36\,\mathrm{k}\Omega$. The arrows indicate the points at which the time series are considered in fig. 4.

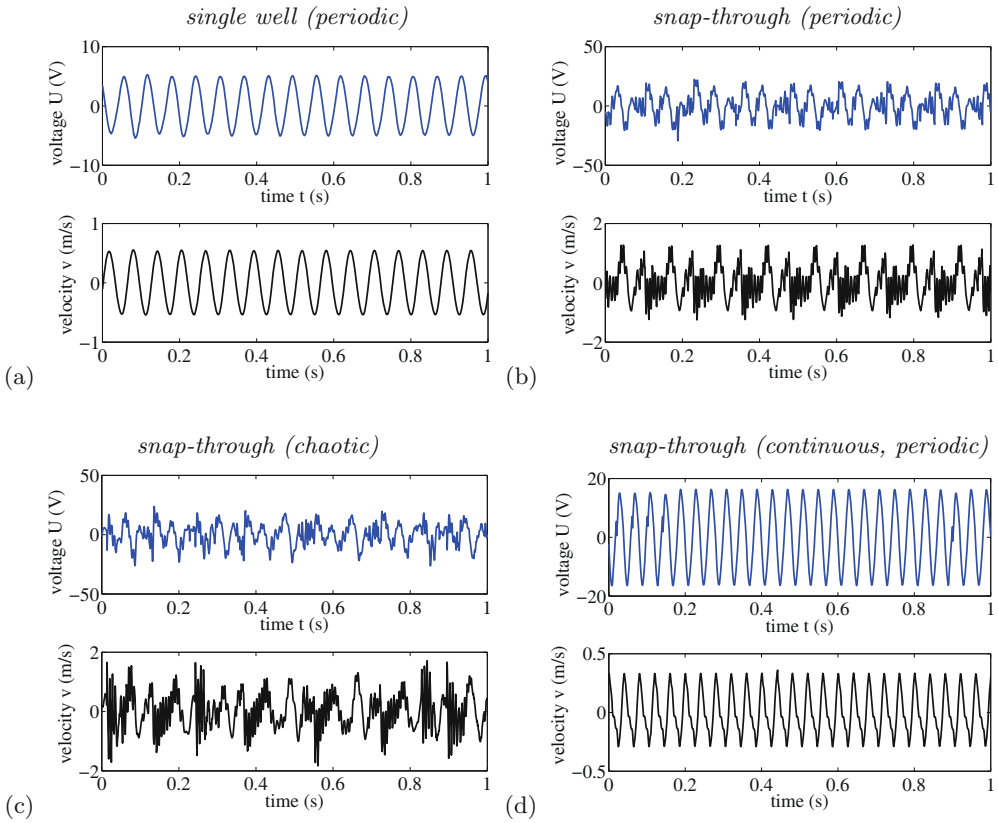

Fig. 4. Velocity and voltage time series for the forcing acceleration amplitude $a_0 = 4g$ with $f = 16\,\mathrm{Hz}$ (a), and $a_0 = 5g$ with three different excitation frequencies $f = 16\,\mathrm{Hz}$ (b), $f = 17\,\mathrm{Hz}$ (c), $f = 25\,\mathrm{Hz}$ (d), respectively. Note that the cases (b) and (c) are characterized by similar voltage/velocity outputs but differ in their periodicity. The corresponding power output $P_{\mathrm{eff}} = 0.4$, 2.4, 2.0, 2.8 mW for cases (a) and (d), respectively.

For clarity, in fig. 5 we show the Fourier transform of the corresponding time series (presented in fig. 4), where the excitation frequencies are clearly observed. For a small amplitude of excitation in fig. 5(a), where the vibration is in a single state, the frequency spectra of voltage and velocity are represented by a single excitation frequency, while in the remaining figures (fig. 5(b)–(d)) one can find additional frequencies. In fig. 5(b) both super- and sub-harmonics can be observed. Figure 5(c) shows a typical non-periodic response and fig. 5(d) exhibits superharmonics. Interestingly, the presence of a small number of superharmonics may indicate snap-through cases (fig. 5(b)–(d)). Clearly, figs.4 and 5 indicate that the bistable cantilever based harvester is exhibiting a range of complex responses such as regular, non-periodic, single well, and snap-through behaviour. The following sections bring attempts to identify the dynamic modes from the voltage and velocity-time series.

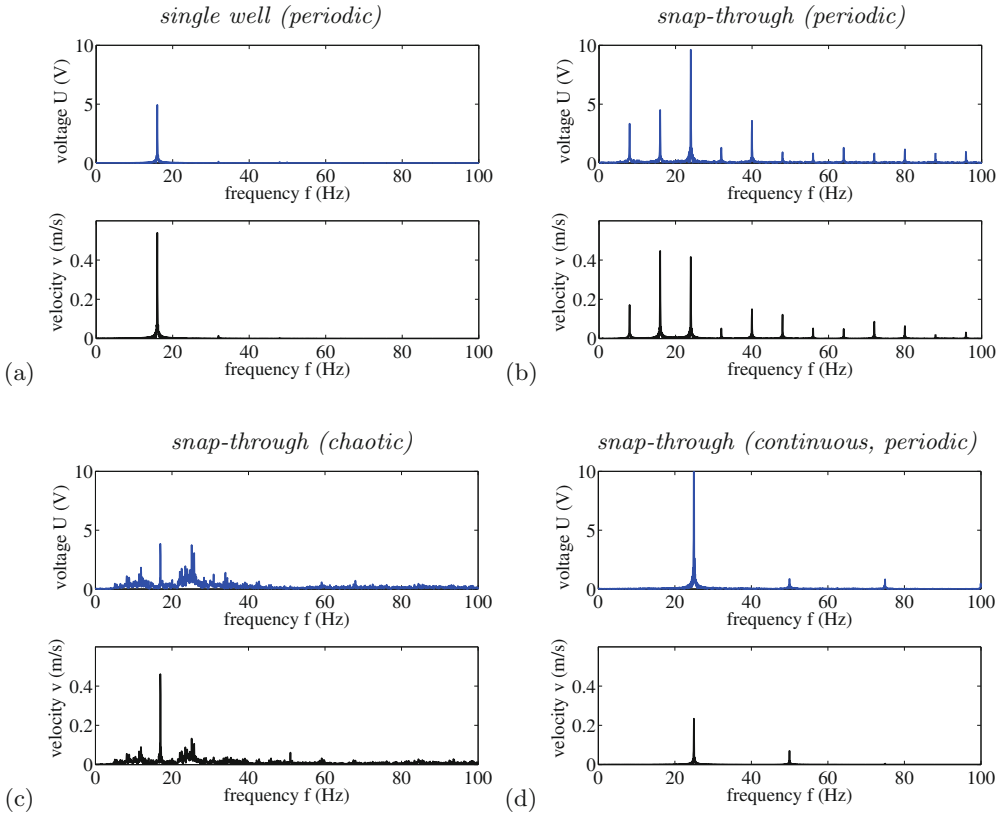

Fig. 5. Fourier spectra of velocity and voltage responses for different excitation frequencies for the same excitation parameters as in fig. 4: (a) $a_0 = 4g$ and $f = 16\,\mathrm{Hz}$ (b); $a_0 = 5g$ and $f = 16\,\mathrm{Hz}$ (b), $f = 17\,\mathrm{Hz}$ (c), $f = 25\,\mathrm{Hz}$ (d).

3 Phase space reconstruction

In the following investigation we plot the discrete return maps using the sampling $\delta t \approx T/4$, where T is the excitation period. Note that this approximately indicates the vanishing of the mutual information [27, 28] which is important for the reconstruction of missing coordinates using the time delay. Such a map simultaneously corresponds to phase portraits.

Note that the proposed sampling corresponds to the correlation delay of the kinematic forcing. The maps are plotted in figs. 6(a)–(d) and the excitation conditions are the same as in figs. 4 and 5. As expected, velocity maps reflect the corresponding voltage maps. The correlations between the delayed coordinates leading to the specific trajectories (figs. 6(a) and (d)) suggest a regular motion of the structure. This is clearly in contrast to fig. 6(c), which is the most random vibration condition. On the other hand, fig. 6(b) can be classified as an intermediate case. This is consistent with the Fourier spectra results (fig. 5(b)) indicating a more complex multifrequency response.

Further analysis of the output response by the method of multiscale entropy and the 0-1 test, used in the next sections —sects. 4 and 5—, will be based on the corresponding voltage output sequences obtained by the same sampling of $\delta t \approx T/4$. The new resampled time series are shown in figs. 7(a)–(d). In both figures (figs. 6 and 7) one can easily distinguish non-periodic behaviour (figs. 6(c) and 7(c)) from the typical regular behaviour (fig. 6(a), (d) and 7(a), (d)). Interestingly, in the case of fig. 7(b) such a presentation can help substantially to classify the response of the harvester as regular vibration.

4 Composite multiscale entropy analysis

To improve our understanding of the behaviour of complex systems that manifest themselves in non-linear behaviour, sample entropy analysis is becoming increasingly popular [17, 29, 30]. This method provides, for measured signals, a relative level of complexity for finite length time series. The complexity definition is associated with "meaningful structural richness" [31, 32] contained over multiple spatio-temporal correlations.

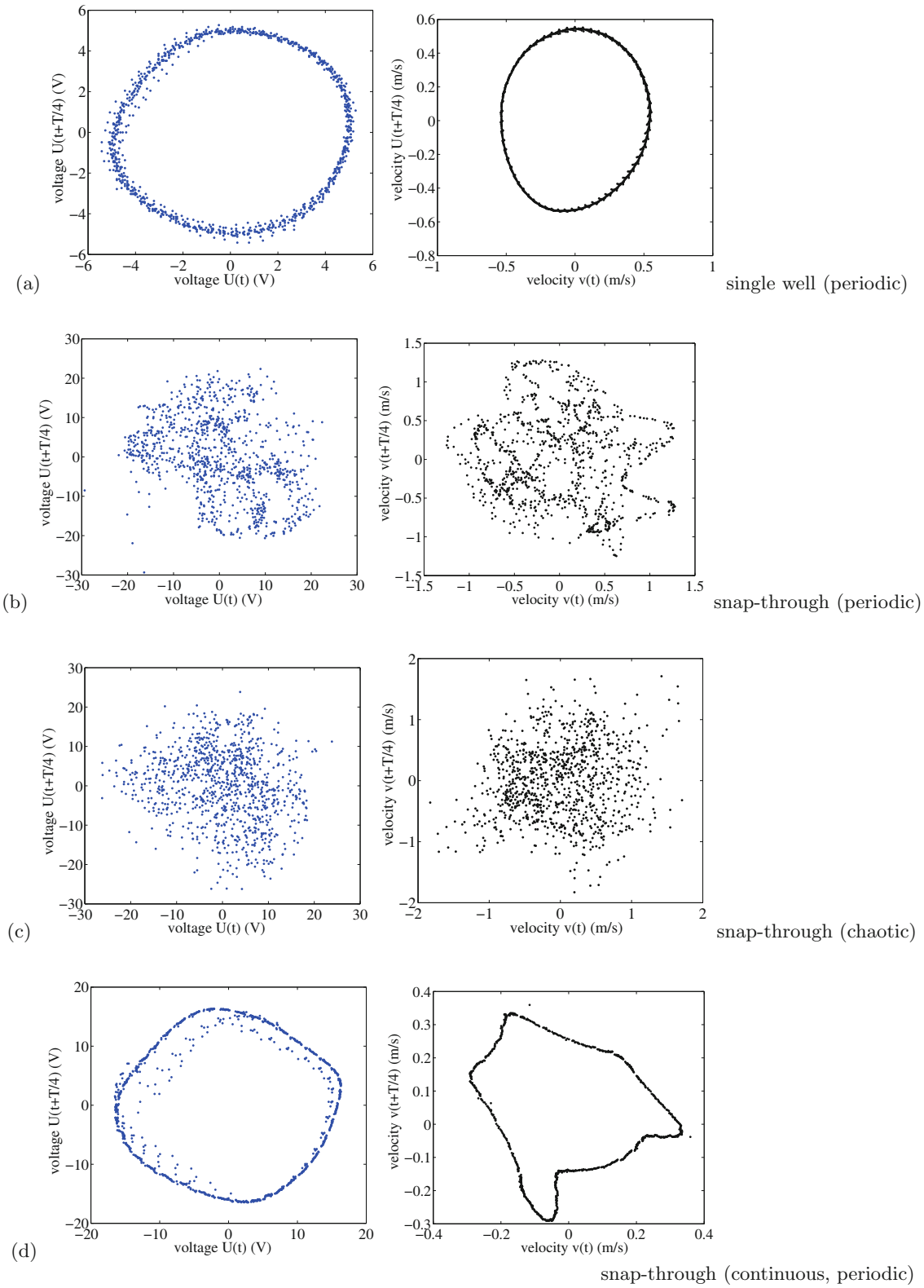

Fig. 6. Phase portraits for velocity $v(t)$ or $v(t+\delta t)$ and voltage output $U(t)$ or $U(t+\delta t)$ sampled with a delay $\delta t \approx T/4$ where $T = 1/f$ is the shaker excitation period. The excitation conditions of a-d as are in figs. 4 and 5.

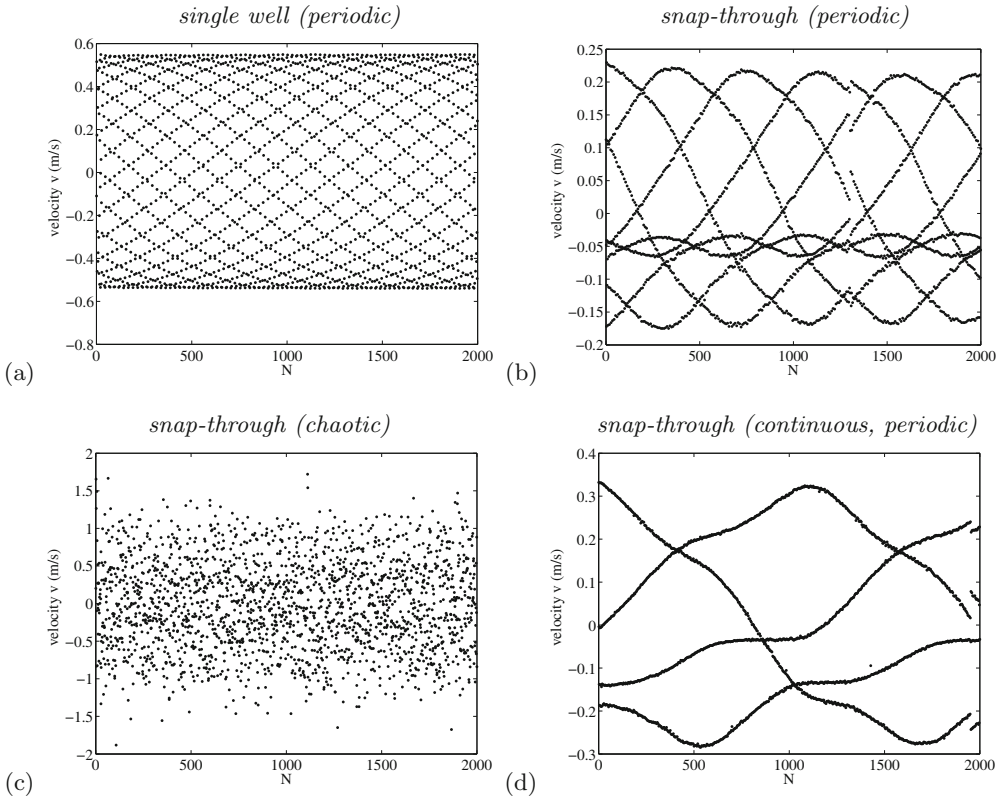

Fig. 7. Sequence of the velocities measured points sampled with $\delta t \approx T/4$ The excitation conditions of a-d as in figs. 4 and 5. N denotes the succeeding sampling index.

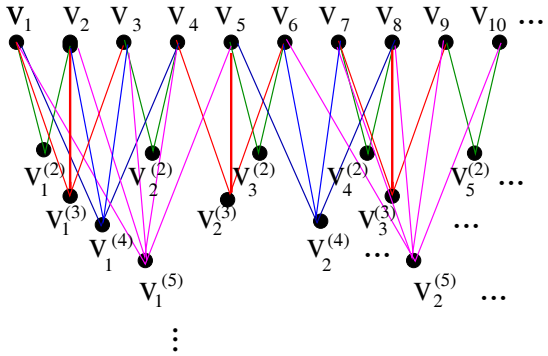

Fig. 8. Scheme of averaging to achieve the effective (coarse-grained) time series of velocity: v_i^τ, where $i = 1..N/\tau$, in the multiscale entropy algorithm (see eq. (2)).

The concept of multi-scale entropy (MSE) [33,34] is based on a coarse-graining procedure that uses a coarse-grained time series as an average of the original data points within non-overlapping windows by increasing the scale factor τ according to the following formula (see fig. 8):

$$v_j^{(\tau)} = \frac{1}{\tau} \sum_{i=(j-1)\tau+1}^{j\tau} v_i, \tag{2}$$

where v is a raw one-dimensional velocity time series $v = \{v_1, v_2, \ldots, v_N\}$. In this approach for each scale factor τ, the MSE calculation is based on the time series of the coarse-grained $v_j^{(\tau)}$:

$$\mathrm{MSE}(\mathbf{v}, \tau, m, r) = \mathrm{SampEn}\left(\mathbf{v}^{(\tau)}, m, r\right), \tag{3}$$

where $m = 2$ is the pattern length and r is the similarity criterion. For the appropriate dynamics identification, it is usually chosen as $r < \sigma$ [35,36], where σ is the standard deviation of the original time series and $v_i^{(1)} = U_i$.

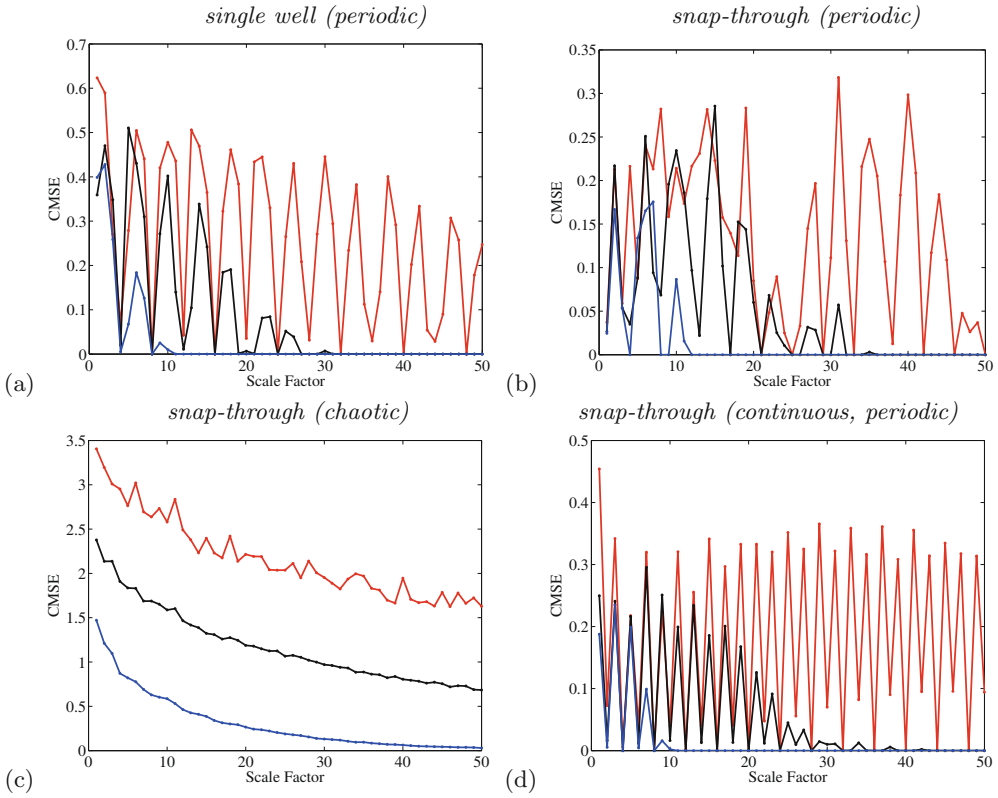

Fig. 9. Composite multiscale entropy calculated for the corresponding velocity sequence of points from fig. 7. The results of CMSE for $m = 2$ and three values of r ($r = \sigma_v$ — blue line, $0.1\sigma_v$ — black line, and $0.01\sigma_v$ — red line).

To estimate SampEn$(\mathbf{v}^{(\tau)}, m, r)$ from eq. (2) (see also fig. 5) we count the number of vector pairs denoted by $v^{(\tau)}(i)$ and $v^{(\tau)}(j)$ in the time series of length m and $m+1$ having distance $d[v^{(\tau)}(i), v^{(\tau)}(j)] < r$. We denote them by P_m and P_{m+1}, respectively. Finally, we define the sample entropy to be [32]

$$\text{SampEn}\left(\mathbf{v}^{(\tau)}, m, r\right) = -\log \frac{P_{m+1}}{P_m}, \tag{4}$$

which can be considered as the minus of the logarithm of the conditional probability that two sequences with a tolerance r form points that remain within r of each other at the next point. However Thuraisingham and Gottwald [37] showed that the functional dependency of MSE on the scale factor τ is highly dependent on the sampling time, and that the same MSE signatures can be found for significantly different dynamic systems.

Continuing these research efforts, Wu *et al.* [38] introduced the concept of a composite multi-scale entropy (CMSE) which for a higher scale factor provides entropy more reliably than the usual multi-scale entropy by including multiple combinations of neighbour points. The prescribed algorithm for CMSE calculations is the following formula:

$$\text{CMSE}(\mathbf{v}, \tau, m, r) = \frac{1}{\tau} \sum_{k=1}^{\tau} \text{SampEn}\left(\mathbf{v}_k^{(\tau)}, m, r\right). \tag{5}$$

In the present paper the CMSE is applied for signals of the bistable system shown by the time series in figs. 2 and 7. Voltage and velocity time series are closely connected; therefore, in the following analysis we limit our analysis to velocity time series which are less affected by noise (see fig. 6). The results of composite multi-scale entropy calculation are usually provided for several similarity factors r for different CMSE values with increasing scale factor τ (fig. 9). The existence of higher values of CMSE corresponds to the existence of more complexity within the analysed signal. It can be noticed that there is a variation in the irregularity of the system as different values of τ are chosen.

The results of the CMSE for $m = 2$ and three values of r ($r = \sigma_v$ —blue line, $0.1\sigma_v$ —black line, and $0.01\sigma_v$ —red line) are presented in fig. 9. Note that the smallest value of CMSE and also its smallest oscillations are reached for the largest similarity factor r. By examination of figs. 9(a)–(d) we observe that in various regions of scale factor, small and large limits of similarity factor r may cause the CMSE to occasionally approach zero. For relatively large r ($r = \sigma_v$ —blue line) this tendency is governed by the period of oscillations that account for strong averaging.

Consequently, the effective (coarse-grained) sequence is averaged out for a certain scale factor, $\tau \gtrsim 15$. The regular-periodic solutions (figs. 9(a), (c), and (d)) show larger fluctuations of CMSE with frequent decreases to small values. Interestingly, reaching fairly small, an almost nodal value is realized for $r = 0.01\sigma_x$. This is a signature that the system is characterised by specific periods (see also figs. 5(a), (c), and (d)). On the other hand, in the chaotic (fig. 9(c)) case we observe a monotonic substantial increase of the CMSE values with decreasing r which is typical for a chaotic response [17, 30]. The slightly decreasing trend of CMSE against the scale factor r indicates long range correlated noise [33] which could be interpreted as an effect of chaotic behaviour. Clearly, the CMSE approach enables us to distinguish the chaotic solution using the criterion of the finite entropy value in the limit of a small similarity factor r. The ability to detect the onset of snap-through of the bistable laminate in a chaotic or continuous (repeatable) manner is of importance to understand the complex dynamics of non-linear harvesting systems and ultimately generate maximum power output for a given broadband ambient vibration.

5 Application of the "0-1 test"

The "0-1 test", invented by Gottwald and Melbourne [39–41], can be applied for any system of a finite dimension to identify the chaotic dynamics but it is based on the statistical properties of a single coordinate only. Thus it is suitable to quantify the response where only one parameter was measured in time. As it is related to the universal properties of the dynamic system, such as spectral measures, it can distinguish a chaotic system from a regular one. In our case, the continuous system (fig. 1) can be described by an embedded space of a higher dimension [28], which can make the analysis more difficult. Here the application of the 0-1 test provides an opportunity to use only a single variable. As expected, the more complex response cases are close to the resonance region (fig. 3).

A particular advantage of the "0-1 test" over the frequency spectrum is that it provides information regarding the dynamics in a single parameter value, similar to the Lyapunov exponent. However, the Lyapunov exponent can be difficult to estimate in any non-smooth simulated or measured data [42]. The present system uses an asymmetric bistable laminate cantilever beam as an example showing non-linear elastic properties. Therefore the 0-1 test can provide the suitable algorithm to identify the chaotic solution [20, 27, 30, 43, 44].

Starting from the measured velocity output $v(i)$ (fig. 4), for sampling points $i = 1, 2, 3, \ldots, N_t$, (where $N_t = 1500$) we define new coordinates $p(n)$ and $q(n)$ as

$$p(n) = \sum_{j=0}^{n} \frac{(v(j) - \overline{v})}{\sigma_u} \cos(jc),$$
$$q(n) = \sum_{j=0}^{n} \frac{(v(j) - \overline{v})}{\sigma_u} \sin(jc), \tag{6}$$

where $\overline{v}$ denotes the average value of v while σ_v its standard deviation, c is a constant $\in [0, \pi]$.

Note that $q(n)$ is a complementary coordinate in the two-dimensional space. Furthermore, starting from the bounded coordinate $v(i)$ we build a new series of $p(n)$ which can be either bounded or unbounded depending on the dynamics of the examined process.

Continuing the calculation procedure, the total mean square displacement is defined as

$$M_c(n) = \lim_{N\to\infty} \frac{1}{N} \sum_{j=1}^{N} \left[(p(j+n) - p(j))^2 + (q(j+n) - q(j))^2 \right], \tag{7}$$

The asymptotic growth of $M_c(n)$ can be easily characterized by the corresponding ratio $K_c'(n)$

$$K_c'(n) = \frac{\ln(M(n))}{\ln n}. \tag{8}$$

Note, our choice of $n_{\max}$ and $N_{\max}$ limits is consistent with that proposed by Gottwald and Melbourne [45–47] $N_{\max}, n_{\max} \to \infty$ but simultaneously $n_{\max}$ should be sufficiently large, $n_{\max} \approx N_{\max}/10$ (for example $n = n_{\max} = 135$ while $N = N_{\max} = 1350$).

In [45, 47] a covariance formulation was used. Implementing it into our case we get

$$K_c = \frac{\operatorname{cov}(\mathbf{X}, \mathbf{M}_c)}{\sqrt{\operatorname{var}(\mathbf{X}) \operatorname{var}(\mathbf{M}_c)}}, \tag{9}$$

where vectors $\mathbf{X} = [1, 2, \ldots, n_{\max}]$, and $\mathbf{M}_c = [M_c(1), M_c(2), \ldots, M_c(n_{\max})]$.

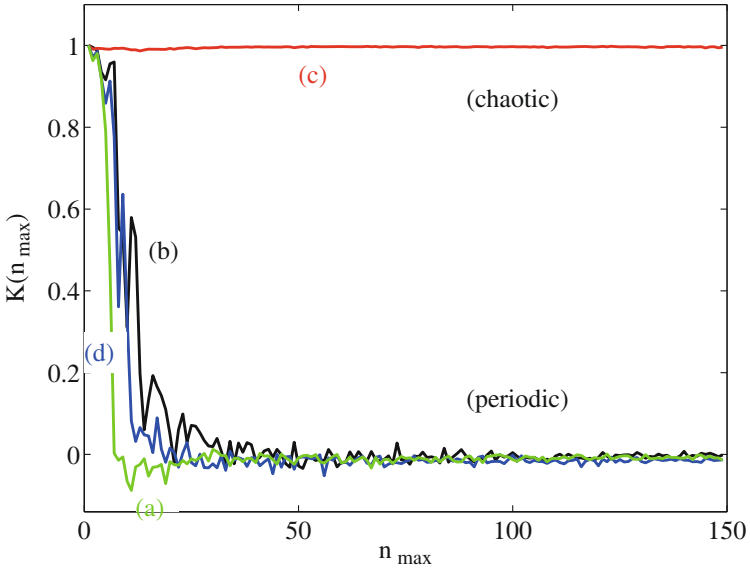

Fig. 10. $K(n_{\max})$ trend (for the fixed $N_{\max} = 1350$). The lines (a)–(d) correspond to cases shown in fig. 7(a)–(d).

The covariance $\mathrm{cov}(\mathbf{x}, \mathbf{y})$ and variance $\mathrm{var}(\mathbf{x})$, for arbitrary vectors $\mathbf{x}$ and $\mathbf{y}$ of $n_{\max}$ elements, and the corresponding averages $\overline{x}$ and $\overline{y}$, respectively, are defined as

$$\mathrm{cov}(\mathbf{x}, \mathbf{y}) = \frac{1}{n_{\max}} \sum_{n=1}^{n_{\max}} (x(n) - \overline{x})(y(n) - \overline{y}),$$
$$\mathrm{var}(\mathbf{x}) = \mathrm{cov}(\mathbf{x}, \mathbf{x}). \tag{10}$$

It is important to note that the parameter c acts like frequency in a spectral calculation. If c is badly chosen, it can resonate with the excitation frequency or its ultra- or sub- harmonics. In the 0-1 test regular motion would yield a ballistic behaviour in the (p, q)-plane [45] and the corresponding $M_c(n)$ results in an asymptotic growth rate even for a regular system. The disadvantage of the test, its strong dependence on the chosen parameter c, can be overcome by a proposed modification. Gottwald and Melbourne [20, 30, 43, 45] suggest to take randomly chosen values of c and compute the median of the corresponding K_c-values.

In fig. 10 we present the results for voltage output of the harvester. Note the asymptotic values for $n_{\max} \in [1, 2, 3, \ldots, 135]$, while $N_{\max} = 1350$, indicate that the cases "a", "b", and "d" (corresponding to figs. 7(a), (b) and (d)) are regular while case "c" (corresponding to fig. 4(c)) is chaotic. Furthermore case "b" decays slowly which could be related to its complex multifrequency nature (see the Fourier spectrum fig. 5(b)). The characteristic slope of decay can be further exploited to distinguish different regular solutions.

6 Conclusions

The application of a bistable laminate beam is considered for piezoelectric-based energy harvesting systems. Based on the experimental time series of a bistable laminate cantilever beam we have examined its dynamic response. The examined system response is shown to have different solutions, with the potential to be exploited in the harvesting device. It is noted that the coexisting solutions of a non-linear energy harvester are characterised by different power outputs. To increase the efficiency of the device one has to identify the wave dynamics along the plate and in the region of piezoelectric transducer.

We demonstrated that the multiscale entropy and "0-1" test can be helpful in the response characterization. A particular benefit of our analysis is that the continuous plate system may be characterised by a single variable (measured voltage and/or displacement) which is an advantage with respect to embedding methods [28]. Using the simple approach of a single point laser vibrometer measurement we note that the multiscale nature of the phenomenon is reflected in the calculated entropy and this method (CMSE) could be used to identify the desired dynamic solution, such as periodic or chaotic response. The presence of a small number of superharmonics also has the potential to identify snap-through. These superharmonics often accompany the regular system response while a vibration amplitude is large enough. Practically, the signal analysis approach, presented above, can be used to identify dynamic modes and optimise an energy harvesting device in the appropriate switching mechanism between solutions.

GL gratefully acknowledges the support of the Polish National Science Center under Grant No. 2012/05/B/ST8/00080. CRB acknowledges funding from the European Research Council under the European Union's Seventh Framework Programme (FP/2007-2013)/ERC Grant Agreement no. 320963 on Novel Energy Materials, Engineering Science and Integrated Systems (NEMESIS). HAK acknowledges financial support from the Engineering and Physical Science Research Council (EPSRC) for Project Reference: EP/J014389/1 "Optimisation of Broadband Energy Harvesters Using Bistable Composites".

References

1. A. Erturk, D.J. Inman, *Piezoelectric Energy Harvesting* (Wiley, London, 2011).
2. R.L. Harne, K.W. Wang, Smart Mat. Struct. **22**, 023001 (2013).
3. M.F. Daqaq, R. Masana, A. Erturk, D.D. Quinn, Appl. Mech. Rev. **66**, 040801 (2014).
4. S.P. Pellegrini, N. Tolou, M. Schenk, J.L. Herder, J. Intell. Mater. Syst. Struct. **24**, 1303 (2013).
5. Y. Wang, L. Peng, Z. Huang, Theor. Appl. Mech. Lett. **5**, 151 (2015).
6. A.F. Arrieta, P. Hagedorn, A. Erturk, D.J. Inman, Appl. Phys. Lett. **97**, 104102 (2010).
7. A.F. Arrieta, T. Delpero, A. Bergamini, P. Ermanni, Appl. Phys. Lett. **102**, 173904 (2013).
8. A.F. Arrieta, T. Delpero, A. Bergamini, P. Ermanni, Proc. SPIE **8688**, 86880G-1 (2013).
9. D.N. Betts, C.R. Bowen, H.A. Kim, N. Gathercole, C.T. Clarke, D.J. Inman, Eur. Phys. J. ST **222**, 1553 (2013).
10. D.N. Betts, H.A. Kim, C.R. Bowen, D.J. Inman, Appl. Phys. Lett. **100**, 114104 (2012).
11. D.N. Betts, H.A. Kim, C.R. Bowen, in *Proceedings of 53rd AIAA/ASME/ASCE/AHS/ASC Structures, Structural Dynamics and Materials Conference* (AIAA, 2012) pp. 2012–1492.
12. D.N. Betts, H.A. Kim, C.R. Bowen, Smart Mater. Res. **2012**, 621364 (2012).
13. D.N. Betts, H.A. Kim, C.R. Bowen, D.J. Inman, Proc. SPIE **8341**, 83412Q-1 (2014).
14. D.N. Betts, C.R. Bowen, H.A. Kim, N. Gathercole, C.T. Clarke, D.J. Inman, Proc. SPIE **8688**, 86881N-1 (2013).
15. A.F. Arrieta, P. Ermanni, Proc. SPIE **9057**, 90570Z-1 (2014).
16. A.F. Arrieta, P. Hagedorn, A. Erturk, D.J.Inamn, in *Proceedings of the ASME 2010 Conference on Conference on Smart Materials, Adaptive Structures and Intelligent Systems, SMASIS2010* (2010).
17. M. Borowiec, A. Rysak, D.N. Betts, C.R. Bowen, H.A. Kim, G. Litak, Eur. Phys. J. Plus **129**, 211 (2014).
18. D.N. Betts, R.A. Guyer, P.-Y. Le Bas, C.R. Bowen, D. Inman, H.A. Kim, in *Proceedings of 55th AIAA/ASMe/ASCE/AHS/SC Structures, Structural Dynamics, and Materials Conference, National Harbor, Maryland 2014*.
19. A.F. Arrieta, P. Ermanni, D.J. Inman, M.A. Karami, in *Proc. of Conference on Smart Materials, Adaptive Structures and Intelligent Systems, ASME 2014*, V002T07A012.
20. A. Syta, C.R. Bowen, H.A. Kim, A. Rysak, G. Litak, Meccanica **50**, 1961 (2015).
21. A.F. Arrieta, T. Delpero, P. Ermanni, in *Proc. ASME 2013 Conference on Smart Materials, Adaptive Structures and Intelligent Systems, SMASIS2013-3137* (2013).
22. P. Harris, C.R. Bowen, H.A. Kim, J. Multifunct. Comp. **3**, 113 (2014).
23. D.N. Betts, C.R. Bowen, D.J. Inman, P.M. Weaver, H.A. Kim, Proc. SPIE **9057**, 90571E-1 (2014).
24. O. Bilgen, Y. Wang, D.J. Inman, Mech. Syst. Signal Proc. **27**, 763 (2012).
25. H.A. Sodano, D.J. Inman, J. Intell. Mater. Syst. Struct. **16**, 799 (2005).
26. H.A. Sodano, J. Lloyd, D.J. Inman, Smart Mater. Struct. **15**, 1211 (2006).
27. G. Litak, A. Syta, M. Wiercigroch, Chaos Solitons Fractals **40**, 2095 (2009).
28. H. Kantz, T. Schreiber, *Non-linear Time Series Analysis* (Cambridge University Press, Cambridge, 1997).
29. M. Borowiec, A.K. Sen, G. Litak, J. Hunicz, G. Koszalka, A. Niewczas, Forsch. Ing. **74**, 99 (2010).
30. G. Litak, S. Schubert, G. Radons, Nonlinear Dyn. **69**, 1255 (2012).
31. P. Grassberger, in *Information Dynamics*, edited by H. Atmanspacher, H. Scheingraber (Plenum Press, New York, 1991) pp. 15–33.
32. J.S. Richman, J.R. Moorman, Am. J. Physiol Heart Circ. Physiol. **278**, H2039 (2000).
33. A.L. Goldberger, L.A.N. Amaral, L. Glass, J.M. Hausdorff, P.Ch. Ivanov, R.G. Mark, J.E. Mietus, G.B. Moody, C.-K. Peng, H.E. Stanley, Circulation **101**, E215 (2000).
34. M. Costa, A.L. Goldberger, C.-K. Peng, Phys. Rev. Lett. **89**, 062102 (2002).
35. M. Costa, C.-K. Peng, A.L. Goldberger, J.M.. Hausdorff, Physica A **330**, 53 (2003).
36. M. Costa, A.L. Goldberger, C.-K. Peng, Phys. Rev. E **71**, 021906 (2005).
37. R.A. Thuraisingham, G.A. Gottwald, Physica A **366**, 323 (2006).
38. S.-D. Wu, C.-W. Wu, S.-G. Lin, C.-C. Wang, K.-Y. Lee, Entropy **15**, 1069 (2013).
39. G.A. Gottwald, I. Melbourne, Proc. R. Soc. London A **460**, 603 (2004).
40. G.A. Gottwald, I. Melbourne, Physica D **212**, 100 (2005).
41. D. Bernardini, G. Litak, J. Braz. Soc. Mech. Sci. Eng., doi:10.1007/s40430-015-0453-y (2016).

42. A. Wolf, J.B. Swift, H.L. Swinney, J.A. Vastano, Physica D **16**, 285 (1985).
43. B. Krese, E. Govekar, Nonlinear Dyn. **67**, 2101 (2012).
44. G. Litak, D. Bernardini, A. Syta, G. Rega, A. Rysak, Eur. Phys. J. ST **222**, 1637 (2013).
45. G.A. Gottwald, I. Melbourne, SIAM J. Appl. Dyn. Syst. **8**, 129 (2009).
46. I. Melbourne, G.A. Gottwald, Nonlinearity **21**, 179 (2008).
47. G.A. Gottwald, I. Melbourne, Nonlinearity **22**, 1367 (2009).